Article

Soft mode dynamics associated with QCD critical point and color superconductivity — pseudogap, anomalous dilepton production and electric conductivity*

Masakiyo Kitazawa[1]* and Teiji Kunihiro [2]

[1] Yukawa Institute for Theoretical Physics, Kyoto University; kitazawa@yukawa.kyoto-u.ac.jp
[2] Yukawa Institute for Theoretical Physics, Kyoto University; kunihiro@yukawa.kyoto-u.ac.jp
* Correspondence: kitazawa@yukawa.kyoto-u.ac.jp

Abstract

We give a systematic account of the soft mode dynamics of QCD critical point(QCD-CP) and the two-flavor color-superconductivity(2SC-CP) based on the 2-flavor Nambu-Jona-Lasinio model, and investigate their effects on electromagnetic observables in relativistic heavy-ion collisions (HIC). We first demonstrate that the collective excitations coupled to the fluctuations of the respective order parameters are the soft modes associated to the respective phase transitions, in the sense that they acquire a prominent spectral strength in the low-energy and low-momentum region above the respective critical temperatures, and the peak energy of the respective spectral functions goes down, i.e., gets softened, and eventually vanishes at the the critical point. It is shown that the diquark soft mode of the 2SC gives rise to the pseudogap, i.e., a depression in the density of states of the quark spectra around the Fermi surface above but in the vicinity of the critical temperature. Then, exploiting the ideas that were developed in condensed matter physics for describing the 'para-conductivity' in the normal phase of metal superconductors, we show that the soft modes cause an anomalous enhancement of electric conductivity and the dilepton production rate, and discuss their relevance to HIC.

Keywords: soft modes: QCD critical point; color-superconductivity; pseudogap; dilepton production rate in heavy-ion collisions; electric conductivity

1. Introduction

One of the central problems in the modern physics is to reveal the properties of hot and dense matter as realized in the cores of compact stars or in the early universe. Since the extremely hot and dense matter should be described in terms of quarks and gluons governed by quantum chromodynamics(QCD), such an effort can be tantamount to developing condensed matter physics in terms of QCD or *QCD-condensed matter physics*. Accumulated theoretical works based on the lattice QCD simulations and low-energy effective theories of QCD show that various types of phase transitions may occur in such a matter [1], which includes the appearance of the color superconductivity (CSC) [2], and the existence of a critical point called QCD critical point (QCD-CP) [3,4] at which a first-order phase-transition line in the higher-density and lower-temperature region ends, and the phase transition turns second order with nonzero current quark masses[1].

*Report numbers: YITP-26-39; J-PARC-TH-0334

[1] In fact, the phase structure around the QCD-CP could be more complicated and might have multiple critical points [5] due to the vector interaction [6], the Kobayashi-Maskawa-'t Hooft (KMT) anomaly term, and mismatched Fermi spheres of the respective pairing particles.

Terrestrial experiments using high-energy heavy-ion collisions (HIC) [7] have been utilized to probe such a hot and dense matter though in nonequilibrium states, and next-generation experimental programs [8] developed or planned in several countries as well as the beam-energy scan experiments [9, 10] intend to focus on dense matter at relatively low temperatures. Since the fluctuation of the order parameter grows in a divergent way as the system approaches the critical point in the normal phase, the observables that are coupled to such a fluctuation should be of primary interest for probing the QCD phase transitions in HIC.

In the case of the QCD-CP [11], since it comes to exist when an explicit chiral symmetry breaking is present at finite baryon density, the order parameter of it is a linear combination of the baryon density and the chiral scalar condensate due to the violation of the charge-conjugation symmetry, as is familiar with Walecka's σ-ω model [12,13]; see Appendix B of the latter paper. Thus, people have been interested in extracting fluctuations or second- and higher-order cumulants of fluctuations of baryon number densities through the event-by-event analyses [9,14,15]. In the present article, we shall, however, focus on the *dynamical* aspects of the fluctuation of the order parameter in the normal phase, say, above the critical temperature, where the dynamical fluctuations of the order parameter has a dominant strength in the *space-like region*. This is the collective particle-hole excitation corresponding to density fluctuations, and has a nature of the soft mode of the QCD-CP in the sense that the peak energy of the collective mode goes down (softens) as the system approaches the QCD-CP in the normal phase and eventually becomes zero there [16–19].

As for the CSC, which is caused by attractive diquark correlations (Cooper pairs) in the presence of Fermi sphere, there are various patterns of CSC due to the intrinsic degrees of freedom of quarks [2]. Among such varieties of the pairing patterns, we only take the two-flavor color superconductivity (2SC) in the present article, and consider the precursory diquark fluctuations, assuming the second-order nature of the phase transition [2]. In fact, it was shown that there exist a specific soft mode in the normal phase of the CSC, which has a prominent spectral support in the space-like region [24–27].

We shall closely examine the spectral properties of these soft modes associated with the respective phase transitions in a coherent way on the basis of the massive 2-flavor and 3-color Nambu-Jona-Lasinio (NJL) model [28–34], basically following Refs. [24–27,35].

Then, we first show that the diquark soft mode of the 2SC causes the *pseudogap in the quark spectra*, i.e., a depression in the density of states of the quark spectra around the Fermi energy, above but in the vicinity of the critical temperature.

Although it is left as a future problem to find good observables to confirm the pseudogap experimentally, we shall show that the soft modes for both phase transitions cause an anomalous enhancement of electric conductivity and the dilepton production rate (DPR) to be observed by HIC. For that, we employ an idea established in condensed matter physics to account for an anomalous excess of the electric conductivity, known as 'para-conductivity' [36–39], in metal superconductors [39,40]. Needless to say, the DPR should be useful to detect the dynamical properties of the created matter by HIC owing to the relatively weak interactions with the surrounding matter, and the significance of electric conductivity in hot and dense quark matter [41–47] has been being revealed for understanding the space-time evolution of the created matter in HIC [48–50].

The present paper is organized as follows. In the next section, we introduce the model Lagrangian, and show the phase diagram given by it in the mean-field approximation. In § 3, a unified account is given of the soft modes as collective excitations based on the linear-response theory, and the important difference in the analytic properties of the spectral functions are elucidated; then, paying attention to the respective analytic properties, we derive the approximate low-energy effective propagators valid in the vicinity of the respective critical points. In § 4, we calculate the density of states of the quark

[2] It should be remarked that gluon fluctuations may alter the order of the phase transition to a (weak) first order from a second one in a relatively low density [20–23]. It seems, however, there is no conclusive claims on the strength of the first-order nature in the low-density region. Thus, we will assume that the phase transition is second-order or weakly first-order in this article.

spectra and establish the emergence of the pseudogap phenomenon. In § 5, we calculate the photon self-energy in the medium by taking account of the soft modes, and demonstrate that the soft modes cause an anomalous enhancement of the electric conductivity and the dilepton production rate near but above the respective critical temperatures of the 2SC and QCD-CP. The last section is devoted to a brief summary and concluding remark.

2. Model Lagrangian and phase diagram

To explore the effects of critical fluctuations in dense quark matter, we employ a simple 2-flavor NJL model with a current quark mass, as was done in Ref. [35],

$$\mathcal{L} = \bar{\psi} i(\not{\partial} - m)\psi + G_S[(\bar{\psi}\psi)^2 + (\bar{\psi} i\gamma_5 \vec{\tau}\psi)^2] + G_D(\bar{\psi} i\gamma_5\tau_2\lambda_A\psi^C)(\bar{\psi}^C i\gamma_5\tau_2\lambda_A\psi), \tag{2.1}$$

where $\psi(x)$ is the quark field and $\psi^C(x) = i\gamma_2\gamma_0\bar{\psi}^T(x)$ denotes its charge conjugation. $\vec{\tau} = (\tau_1, \tau_2, \tau_3)$ are the Pauli matrices for the flavor $SU(2)_f$, and λ_A $(A = 2, 5, 7)$ are the antisymmetric components of the Gell-Mann matrices for the color $SU(3)_c$. The scalar coupling constant G_S and the three-momentum cutoff Λ are determined so as to reproduce the pion mass $m_\pi = 138$ MeV and the pion decay constant $f_\pi = 93$ MeV at the current quark mass $m = 5.5$ MeV [32]: $G_S = 5.50\ \mathrm{GeV}^{-2}$ and $\Lambda = 631$ MeV. We treat G_D as a free parameter and vary it in the range obtained by various estimates [34].

To describe the chiral restoration and the onset of the 2SC phase, we adopt the mean-field approximation (MFA) for the scalar and diquark operators,

$$\hat{\sigma}(\boldsymbol{x}, t) = \bar{\psi}(\boldsymbol{x}, t)\psi(\boldsymbol{x}, t) \qquad \text{and} \qquad \hat{\delta}_A(\boldsymbol{x}, t) = \bar{\psi}^C(\boldsymbol{x}, t) i\gamma_5\tau_2\lambda_A\psi(\boldsymbol{x}, t), \tag{2.2}$$

and their respective expectation values $\langle\hat{\sigma}\rangle$ and $\langle\hat{\delta}_A\rangle$ are called the chiral and diquark condensates, respectively. The Lagrangian density in this approximation takes the form

$$\mathcal{L}_{\mathrm{MFA}} = \bar{\psi} i(\not{\partial} - m)\psi - M\bar{\psi}\psi - \frac{1}{2}(\Delta^\dagger \bar{\psi}^C i\gamma_5\tau_2\lambda_A\psi + \mathrm{h.c.}) - \frac{M^2}{4G_S} - \frac{|\Delta|^2}{4G_D}, \tag{2.3}$$

with $M = -2G_S\langle\hat{\sigma}\rangle$ and $\Delta = -2G_D\langle\hat{\delta}_A\rangle$.

From Eq. (2.3), the thermodynamic potential per unit volume at temperature T and quark chemical potential μ is calculated to be [25]

$$\begin{aligned}\omega_{\mathrm{MFA}} = \frac{(M-m)^2}{4G_S} + \frac{|\Delta|^2}{4G_D} - 4\int\frac{d^3p}{(2\pi)^3}\Big\{ & E_{\boldsymbol{p}} + T\log\big(1 + e^{-\xi_+/T}\big)\big(1 + e^{-\xi_-/T}\big) \\ & + \epsilon_+ + \mathrm{sgn}(\xi_-)\epsilon_- + 2T\log\big(1 + e^{-\epsilon_+/T}\big)\big(1 + e^{-\mathrm{sgn}(\xi_-)\epsilon_-/T}\big)\Big\},\end{aligned} \tag{2.4}$$

$$E_{\boldsymbol{p}} = \sqrt{\boldsymbol{p}^2 + M^2}, \qquad \xi_\pm = E_{\boldsymbol{p}} \pm \mu, \qquad \epsilon_\pm = \sqrt{\xi_\pm^2 + |\Delta|^2}. \tag{2.5}$$

The expectation values M and Δ in the equilibrium state are given by minimizing ω_{MFA}, and the stationary condition to it gives the 'gap equations'

$$\frac{\partial\omega_{\mathrm{MFA}}}{\partial M} = 0, \qquad \frac{\partial\omega_{\mathrm{MFA}}}{\partial\Delta} = 0. \tag{2.6}$$

The 2SC phase is characterized by a nonzero diquark condensate Δ. At the 2SC-PT, Δ in the 2SC phase gets to have a non-zero value continuously from zero, provided that the PT is of the second order, which implies that ω_{MFA} satisfies

$$\frac{\partial^2\omega_{\mathrm{MFA}}}{\partial\Delta^2}\Big|_{\Delta=0} = 0, \tag{2.7}$$

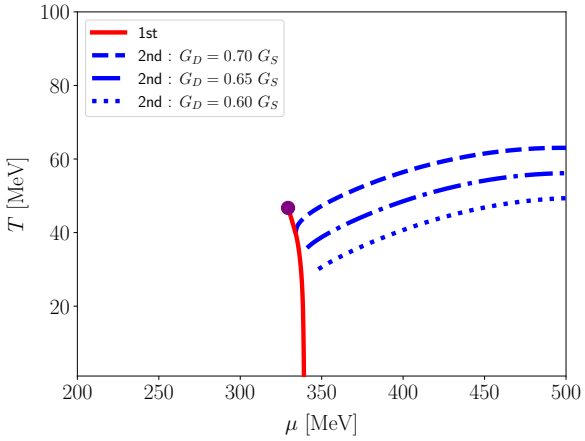

Figure 1. Phase diagram calculated by the mean-field approximation in the 2-flavor NJL model (2.1) [35]. The solid line shows the first-order phase transition calculated with $G_D = 0.70 G_S$. The dashed, dash-dotted, and dotted lines are the second-order 2SC-PT for $G_D/G_S = 0.70$, 0.65, and 0.60, respectively. The QCD-CP is indicated by the circle marker located at $(T_{\rm CP}, \mu_{\rm CP}) \simeq (46.712, 329.34)$ MeV.

at the 2SC-PT. Equation (2.7) tells us that the thermodynamic potential around the minimum point is flat, and hence the diquark susceptibility $\chi_D = (\partial^2 \omega_{\rm MFA}/\partial \Delta^2)^{-1}$ is divergent, and accordingly so do the fluctuations of Δ at the 2SC-PT. Such divergences are a general feature of second-order phase transitions [14]. We will discuss their consequences in subsequent sections. Owing to the nonzero current quark mass, the chiral condensate $\langle \hat{\sigma} \rangle$ is always nonzero. On the other hand, when $\omega_{\rm MFA}$ has two local minima, the values of M and Δ at the global minimum can show a discontinuous change when T and μ are varied, which corresponds to a first-order phase transition.

In Fig. 1, we show the phase diagram in the T–μ plane obtained by the MFA [35]: The solid line shows the first-order transition line. The circle marker at $(T_{\rm CP}, \mu_{\rm CP}) \simeq (46.712, 329.34)$ MeV denotes the endpoint of the first-order transition line, at which the phase transition is of second order and called the QCD-CP. The dashed, dash-dotted, and dotted lines show the 2SC-PT for $G_D/G_S = 0.70$, 0.65, and 0.60, respectively. The critical temperature of the 2SC-PT increases as G_D becomes larger. The 2SC-PT is of second order in our model.

As mentioned in Introduction, several studies beyond the MFA suggest that the order of the 2SC-PT is a weak first order owing to fluctuations of gluon fields [20,21,23]. Since any global symmetry distinguishing the 2SC phase from the normal one is absent, the transition to the 2SC phase may have to be crossover [2]. In any event, we are not aware of a definite conclusion on the order of the 2SC-PT so far, the following analyses will be performed simply based on the result of the MFA.

At the QCD-CP where two minima of $\omega_{\rm MFA}$ existing in the lower-T and higher-μ region merge, $\omega_{\rm MFA}$ has a flat direction on the M–Δ plane. As Fig. 1 shows, in our model $\Delta = 0$ is satisfied at the QCD-CP and the flat direction is along M direction. Therefore, at the minimum $\omega_{\rm MFA}$ satisfies

$$\frac{\partial^2 \omega_{\rm MFA}}{\partial M^2} = 0, \tag{2.8}$$

at the QCD-CP. Equation (2.7) shows that the fluctuation of M is divergent at the QCD-CP.

3. Collective diquark/particle-hole excitations as the soft modes of the phase transitions

In this section, we discuss the dynamical properties of fluctuations of Δ and M near the 2SC-PT and QCD-CP, respectively, based on the linear response theory. We show that these fields exhibit collective excitations with prominent peaks of the strength function near these phase transitions, respectively [16,17,24,25,35].

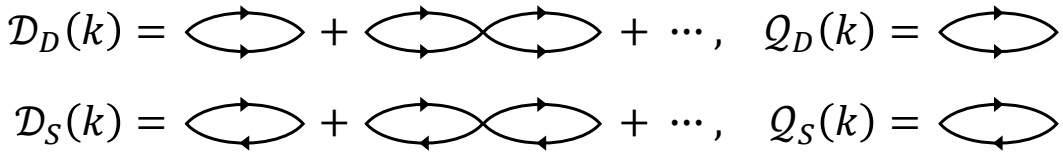

Figure 2. Diagrammatic representation of Eq. (3.12). The single lines denote the quark propagator.

3.1. Linear response theory

The linear-response theory [51] is a useful tool to explore dynamical properties of collective excitations. A key idea of this theory is to disturb the system with an infinitesimal external field represented by the Hamiltonian $H_{\rm ext} = \int d^3x dt e^{i\omega t - i\boldsymbol{k}\cdot\boldsymbol{x}} f(\boldsymbol{x},t)\mathcal{O}(\boldsymbol{x},t)$, where $\mathcal{O}(\boldsymbol{x},t)$ is a bosonic-field operator and $f(\boldsymbol{x},t)$ is a classical function. As a result of applying the external field, the expectation value of $\mathcal{O}(\boldsymbol{x},t)$ can deviate from its thermal expectation value $\langle\mathcal{O}\rangle$. For an infinitesimal perturbation, this deviation is proportional to $f(\boldsymbol{x},t)$ and represented by [51]

$$\delta\langle\mathcal{O}(\boldsymbol{x},t)\rangle \equiv \langle\mathcal{O}(\boldsymbol{x},t)\rangle_{\rm ext} - \langle\mathcal{O}\rangle = \int d^3x' dt' D^R(\boldsymbol{x}-\boldsymbol{x}', t-t') f(\boldsymbol{x}',t'), \tag{3.9}$$

where $\langle\mathcal{O}(\boldsymbol{x},t)\rangle_{\rm ext}$ represents the expectation value with the external field and $D^R(\boldsymbol{x},t)$ is the retarded Green's function

$$D^R(\boldsymbol{x},t) = -i\langle[\mathcal{O}(\boldsymbol{x},t), \mathcal{O}(\boldsymbol{0},0)]\rangle\theta(t), \tag{3.10}$$

with $[A,\, B] = AB - BA$ being the commutator. The Fourier transformation of Eq. (3.9) leads to

$$\delta\langle\mathcal{O}(\boldsymbol{k},\omega)\rangle = D^R(\boldsymbol{k},\omega) f(\boldsymbol{k},\omega), \tag{3.11}$$

with $D^R(\boldsymbol{k},\omega) = \int d^3x dt e^{i\omega t - i\boldsymbol{k}\cdot\boldsymbol{x}} D^R(\boldsymbol{x},t)$ and so on.

When $D^R(\boldsymbol{k},\omega)$ has a pole at $\omega = \omega(\boldsymbol{k})$ for real ω, Eq. (3.11) tells us that $\delta\langle\mathcal{O}(\boldsymbol{k},\omega(\boldsymbol{k}))\rangle$ becomes nonzero with an infinitesimal external perturbation. Such a mode forms a collective excitation that carries the quantum number of the operator $\mathcal{O}(\boldsymbol{x},t)$. When $D^R(\boldsymbol{k},\omega)$ admits a complex pole $\omega = \omega(\boldsymbol{k}) \in \mathbb{C}$ with a small imaginary part, it is also said that there exists a well-developed collective mode or quasi particle.

To explore the fluctuations of Δ and M, we only have to substitute the operators $\hat{\delta}_A(\boldsymbol{x},t)$ and $\hat{\sigma}(\boldsymbol{x},t)$ into $\hat{\mathcal{O}}(\boldsymbol{x},t)$, respectively. We denote these retarded functions as $D_D^R(\boldsymbol{k},\omega)$ and $D_S^R(\boldsymbol{k},\omega)$, respectively.

3.2. Random-phase approximation and Thouless criterion

The retarded Green's functions $D_D^R(\boldsymbol{k},\omega)$ and $D_S^R(\boldsymbol{k},\omega)$ that are consistent with the MFA are given by the random-phase approximation (RPA) or ring approximation,

$$D_\gamma^R(\boldsymbol{k},\omega) = \frac{Q_\gamma^R(\boldsymbol{k},\omega)}{1 + G_\gamma Q_\gamma^R(\boldsymbol{k},\omega)} = Q_\gamma^R(\boldsymbol{k},\omega) - Q_\gamma^R(\boldsymbol{k},\omega) G_\gamma Q_\gamma^R(\boldsymbol{k},\omega) + \cdots, \tag{3.12}$$

with $\gamma = D, S$ and the unperturbed correlation functions $Q_\gamma^R(\boldsymbol{k},\omega)$. As shown in Fig. 2, $Q_\gamma^R(\boldsymbol{k},\omega)$ are represented by the one-loop graphs, where the direction of a quark propagator is opposite for $\gamma = D, S$.

To calculate $Q^R_\gamma(\boldsymbol{k},\omega)$, it is convenient to first introduce the corresponding functions in the Matsubara (imaginary-time) formalism

$$\begin{aligned}\mathcal{Q}_D(k) &= \int d^3x d\tau e^{i\nu_n\tau - i\boldsymbol{k}\cdot\boldsymbol{x}}\langle T_\tau \hat{\delta}_A(\boldsymbol{x},\tau)\hat{\delta}^\dagger_A(\boldsymbol{0},0)\rangle_{\rm free} \\ &= -2N_f(N_c-1)\int_p {\rm Tr}_D[\mathcal{G}_0(p)\mathcal{G}_0(k-p)], \qquad (3.13)\\ \mathcal{Q}_S(k) &= \int d^3x d\tau e^{i\nu_n\tau - i\boldsymbol{k}\cdot\boldsymbol{x}}\langle T_\tau \hat{\sigma}(\boldsymbol{x},\tau)\hat{\sigma}(\boldsymbol{0},0)\rangle_{\rm free} \\ &= -2N_f N_c\int_p {\rm Tr}_D[\mathcal{G}_0(p)\mathcal{G}_0(k+p)], \qquad (3.14)\end{aligned}$$

where $k=(\boldsymbol{k},i\nu_n)$ is the collective index with $\nu_n = 2n\pi/T$ the Matsubara frequency for bosons, $\langle\cdot\rangle_{\rm free}$ denotes the expectation value in the non-interacting system, and $\mathcal{G}_0(p) = \mathcal{G}_0(\boldsymbol{p},i\omega_m) = 1/[(i\omega_m+\mu)\gamma_0 - \boldsymbol{p}\cdot\boldsymbol{\gamma} - M]$ is the free-quark propagator with $\omega_m = (2m+1)\pi/T$ being the Matsubara frequency for fermions. The retarded functions $Q^R_\gamma(\boldsymbol{k},\omega)$ is then obtained by the analytic continuation $i\nu_n \to \omega + i\eta$

$$\mathcal{Q}_\gamma(k) = \mathcal{Q}_\gamma(\boldsymbol{k},i\nu_n) \xrightarrow[i\nu_n\to\omega+i\eta]{} Q^R_\gamma(\boldsymbol{k},\omega). \qquad (3.15)$$

For later convenience, we also introduce the retarded T-matrices

$$\Xi^R_\gamma(\boldsymbol{k},\omega) = \frac{1}{G_\gamma^{-1} + Q^R_\gamma(\boldsymbol{k},\omega)} = G_\gamma - G_\gamma D^R_\gamma(\boldsymbol{k},\omega)G_\gamma, \qquad (3.16)$$

which also means

$$D^R_\gamma(\boldsymbol{k},\omega) = G_\gamma^{-1}Q^R_\gamma(\boldsymbol{k},\omega)\Xi^R_\gamma(\boldsymbol{k},\omega). \qquad (3.17)$$

An important property of the T-matrices (3.16) is that their low-energy low-momentum limits are related to the second derivatives of $\omega_{\rm MFA}$ as

$$\lim_{|\boldsymbol{k}|\to 0}{\Xi^R_D}^{-1}(\boldsymbol{k},0) = 2\frac{\partial^2\omega_{\rm MFA}}{\partial\Delta^2}, \qquad \lim_{|\boldsymbol{k}|\to 0}{\Xi^R_S}^{-1}(\boldsymbol{k},0) = 2\frac{\partial^2\omega_{\rm MFA}}{\partial M^2}, \qquad (3.18)$$

as one can readily verify [35]. Since the thermodynamic potential satisfies $\partial^2\omega_{\rm MFA}/\partial\Delta^2 = 0$ ($\partial^2\omega_{\rm MFA}/\partial M^2 = 0$) at the 2SC-PT (QCD-CP) as discussed in Sec. 2, from Eq. (3.18) it is immediately concluded that

$$\Xi^{R\,-1}_\gamma(\boldsymbol{0},0) = 0 \quad \text{and} \quad D^{R\,-1}_\gamma(\boldsymbol{0},0) = 0, \qquad (3.19)$$

are satisfied at the respective critical points. These properties are called the Thouless criterion [52]. Although the derivation of the Thouless criterion presented here relies on the MFA and the RPA, it has a general validity beyond the MFA, reflecting the fact that $\lim_{|\boldsymbol{k}|\to 0}\Xi^{R\,-1}_\gamma(\boldsymbol{k},0)$ corresponds to the susceptibility of the order-parameter field that diverges at the second-order phase transition [39].

An important consequence of the Thouless criterion is that $D^R_D(\boldsymbol{k},\omega)$ and $D^R_S(\boldsymbol{k},\omega)$ have a *massless pole* $\omega(\boldsymbol{0}) = 0$ at the 2SC-PT and QCD-CP, respectively. Since the location of the pole $\omega(\boldsymbol{k})$ changes continuously as a function of T and μ, the pole stays near the origin $\omega = 0$ even away from the transition point. Such a mode is called the *soft mode* of the respective phase transitions.

3.3. Analytic structure of Q^R_γ

The imaginary parts of $Q^R_\gamma(\boldsymbol{k},\omega)$ are calculated to be [35]

$$\begin{aligned}\mathrm{Im}Q^R_D(\boldsymbol{k},\omega) = &-\frac{N_f(N_c-1)T}{4\pi}\frac{(\omega+2\mu)^2-\boldsymbol{k}^2}{|\boldsymbol{k}|}\\ &\times\Big\{\theta\big(\bar\Lambda-|\omega+2\mu|\big)\theta\big(|\omega+2\mu|-\sqrt{\boldsymbol{k}^2+4M^2}\big)F_D\big(\omega,\bar k(|\boldsymbol{k}|,\omega+2\mu)\big)\\ &\quad+\theta\big(\bar k(|\boldsymbol{k}|,\bar\Lambda)-|\omega+2\mu|\big)\Big[F_D\big(\omega,\bar k(|\boldsymbol{k}|,\omega+2\mu)\big)-F_D\big(\omega,\bar\Lambda\big)\Big]\Big\},\end{aligned}\tag{3.20}$$

$$F_D(\omega,x) = 2\sum_{s=\pm} s\log\cosh([\omega+sx]/4T),\tag{3.21}$$

and

$$\begin{aligned}\mathrm{Im}Q^R_S(\boldsymbol{k},\omega) = &-\frac{N_fN_cT}{4\pi}\frac{\omega^2-\boldsymbol{k}^2-4M^2}{|\boldsymbol{k}|}\\ &\times\Big\{\theta\big(\bar\Lambda-|\omega|\big)\theta\big(|\omega|-\sqrt{\boldsymbol{k}^2+4M^2}\big)F_S\big(\omega,\bar k(|\boldsymbol{k}|,\omega)\big)\\ &\quad+\theta\big(\bar k(|\boldsymbol{k}|,\bar\Lambda)-|\omega|\big)\Big[F_S\big(\omega,\bar k(|\boldsymbol{k}|,\omega)\big)-F_S\big(\omega,\bar\Lambda\big)\Big]\Big\},\end{aligned}\tag{3.22}$$

$$F_S(\omega,x) = \sum_{s,t=\pm} s\log\cosh([\omega+sx-2t\mu]/4T).\tag{3.23}$$

From Eqs. (3.20) and (3.22), one finds that the first (second) term in the curly bracket in Eq. (3.20) takes a nonzero value at

$$|\omega+2\mu| > \sqrt{\boldsymbol{k}^2+4M^2},\qquad (|\omega+2\mu|<\bar k(|\boldsymbol{k}|,\bar\Lambda)),\tag{3.24}$$

while that in Eq. (3.22) is nonzero at

$$|\omega| > \sqrt{\boldsymbol{k}^2+4M^2},\qquad (|\omega|<\bar k(|\boldsymbol{k}|,\bar\Lambda)).\tag{3.25}$$

One can also verify from Eqs. (3.20) and (3.22) that $Q^R_D(\boldsymbol{k},\omega)$ and $Q^R_S(\boldsymbol{k},\omega)$ are not analytic at the boundary of the supports (3.24) and (3.25). Therefore, $Q^R_S(\boldsymbol{k},\omega)$ is not analytic at the origin, whereas $Q^R_D(\boldsymbol{k},\omega)$ is analytic there. As we will see later, this leads to a qualitative difference in the nature of the soft modes of the 2SC-PT and QCD-CP.

Here we would like to clear up the confusion, if not misunderstanding, seen in the literature about of the nature of the soft mode associated to the QCD-CP. As discussed in Sec. 3.2, $D^R_S(\boldsymbol{k},\omega)$ is not analytic at the origin in contrast to $D^R_D(\boldsymbol{k},\omega)$. This difference does down to that of the dynamical structure factors; although $S_D(\boldsymbol{k},\omega)$ is an analytic around the origin, $S_S(\boldsymbol{k},\omega)$ is not and has different limiting values at the origin depending on whether approaching in the space-like or time-like region. The pole existing in the space-like region represent mostly the density fluctuations consisting of (quark) particle-hole excitations, and does move toward the origin in the complex energy plane as the system approaches the critical point, showing the very nature of the soft mode [16,17]. There are also poles in $D^R_S(\boldsymbol{k},\omega)$ in the time-like region, which are the mesonic excitations such as the σ and π and do not show any softening behavior. Indeed, the support of the spectral function in the time-like region for $S_S(\boldsymbol{k},\omega)$ exist only in the region $|\omega| > \sqrt{\boldsymbol{k}^2+4M^2}$, which never becomes zero because M stays nonzero at the QCD-CP. Thus, it might be confusing, if not inadequate, to denote the soft mode of the QCD-CP by the symbol σ as seen in some literature; a possible substitute may be σ_s with s being short for 'sound'.

3.4. Linearized time-dependent Ginzburg-Landau (TDGL) approximation

In this subsection, we derive effective equations for the soft modes near the 2SC-PT and QCD-CP known as the linearized time-dependent Ginzburg-Landau (TDGL) equations [35]. These equations are obtained by expanding $\Xi^R_\gamma(\boldsymbol{k},\omega)$ with respect to $\boldsymbol{k}$ and ω. in the way of the derivation, the qualitative difference will become apparent in the analytic properties of the soft modes of the 2SC-PT and QCD-CP. The resultant TDGL equations will be found helpful to investigate the effects of the soft modes on various observables in a simple way to be done in the subsequent sections.

3.4.1. Soft modes of 2SC-PT

Let us start with the soft mode of the 2SC-PT, which is a collective mode encoded in $\Xi^R_D(\boldsymbol{k},\omega)$. As discussed in Sec. 3.2, this T-matrix satisfies ${\Xi^R_D}^{-1}(\boldsymbol{0},0)=0$ at $T=T_c$ and is analytic at $\omega=|\boldsymbol{k}|=0$. Therefore, at small ω and $|\boldsymbol{k}|$ this function is well approximated by the Taylor expansion

$$ {\Xi^R_D}^{-1}(\boldsymbol{k},\omega) \simeq A_D(\boldsymbol{k}) + C_D\omega, \tag{3.26} $$

near the 2SC-PT with

$$ A_D(\boldsymbol{k}) = G_D^{-1} + Q^R_D(\boldsymbol{k},0), \qquad C_D = \left.\frac{\partial Q^R_D(\boldsymbol{0},\omega)}{\partial\omega}\right|_{\omega=0}, \tag{3.27} $$

which are found to be real and complex numbers, respectively. Since the Thouless criterion (3.18) tells us that $A_D(\boldsymbol{0})=0$ at $T=T_c$, Eq. (3.26) is further expanded as

$$ {\Xi^R_D}^{-1}(\boldsymbol{k},\omega) \simeq \tilde{a}_D\epsilon + b_D\boldsymbol{k}^2 + c_D\omega, \tag{3.28} $$

with the reduced temperature

$$ \epsilon = \frac{T-T_c}{T_c}. \tag{3.29} $$

The approximate formula (3.28) corresponds to the linearized time-dependent Ginzburg-Landau (TDGL) equation [39]. In fact, the linear-response theory, Eq. (3.11), shows that the equation of motion of the field Δ with an infinitesimal external field is given by ${\Xi^R_D}^{-1}(\boldsymbol{k},\omega)\Delta(\boldsymbol{k},\omega)=0$, whose Fourier transformation gives the linearized TDGL equation $(iC_D\partial/\partial\omega - b_D\nabla^2 + \tilde{a}_D\epsilon)\Delta=0$. In the following, we refer to Eqs. (3.28) and (3.26) as the TDGL and the low-energy (LE) approximations, respectively. It is numerically verified that these approximations well reproduce the ${\Xi^R_D}^{-1}(\boldsymbol{k},\omega)$ obtained in the RPA near the 2SC-PT [35].

From Eq. (3.28), the dispersion relation of the soft mode is readily obtained as

$$ \omega = -(\tilde{a}_D\epsilon + b_D\boldsymbol{k}^2)/c_D. \tag{3.30} $$

When $|\mathrm{Re}c_D| \ll |\mathrm{Im}c_D|$, Eq. (3.28) can be rewritten as

$$ \Xi^R_D(\boldsymbol{k},\omega) = \frac{1}{a_D + b_D\boldsymbol{k}^2 + c_D\omega} = \frac{i}{|\mathrm{Im}c_D|}\frac{1}{\omega + i\tau_{\mathrm{GL}}^{-1}\left(1+\xi_D^2\boldsymbol{q}^2\right)}, \tag{3.31} $$

where $\tau_{\mathrm{GL}} = |c_D|/a_D$ and $\xi_D = \sqrt{b_D/a_D}$ are the relaxation time and the coherence length of the soft mode, respectively. Equation (3.31) shows that the soft mode is a damping mode.

Using the approximations $M \ll T+|\mu| \ll \Lambda$ and $T/\mu \ll 1$, the coefficients in Eq. (3.28) are calculated to be

$$ \tilde{a}_D = \frac{2N_f(N_c-1)}{\pi^2}\mu^2, \quad b_D = \frac{7N_f(N_c-1)\zeta(3)}{48\pi^4}\frac{\mu^2}{T^2}, \quad c_D = -i\frac{N_f(N_c-1)}{4\pi}\frac{\mu^2}{T}, \tag{3.32} $$

up to logarithmic terms [35]. On account of Eq. (3.32), the expressions of the relaxation time and the coherence length in Eq. (3.31) are simplified to

$$\tau_{\rm GL} = \frac{\pi}{8T}\frac{1}{\epsilon}, \qquad \xi_D = \sqrt{\frac{7\zeta(3)}{96T^2}}\frac{1}{\epsilon^{1/2}}, \tag{3.33}$$

respectively. One sees that the both quantities do not depend on μ and are divergent for $\epsilon \to 0$.

3.4.2. Soft mode of QCD-CP

The soft mode of the QCD-CP can be treated in much the same way as the 2SC-PT. $\Xi_S^R(\boldsymbol{k},\omega)$ is approximated for small ω and $|\boldsymbol{k}|$ as

$$\Xi_S^{R\,-1}(\boldsymbol{k},\omega) \simeq A_S(\boldsymbol{k}) + C_S(\boldsymbol{k})\omega, \tag{3.34}$$

with

$$A_S(\boldsymbol{k}) = G_S^{-1} + Q_S^R(\boldsymbol{k},0) \quad \text{and} \quad C_S(\boldsymbol{k}) = \left.\frac{\partial Q_S^R(\boldsymbol{k},\omega)}{\partial\omega}\right|_{\omega=0}, \tag{3.35}$$

which are found to be real and pure imaginary, respectively. An important difference of Eq. (3.35) from Eq. (3.26) is that $\Xi_S^{R\,-1}(\boldsymbol{k},\omega)$ is not analytic at $\omega = |\boldsymbol{k}| = 0$; reflecting it, $C_S(\boldsymbol{k})$ diverges as $1/|\boldsymbol{k}|$ for $\boldsymbol{k} \to \boldsymbol{0}$. As discussed in Sec. 3.3, $\Xi_S^R(\boldsymbol{k},\omega)$ has discontinuities at $|\omega| = \bar{k}(|\boldsymbol{k}|,\bar{\Lambda}) \simeq |\boldsymbol{k}|$. Therefore, the LE approximation (3.34) is valid only in the region $|\omega| < \bar{k}(|\boldsymbol{k}|,\bar{\Lambda})$ and not applicable to the time-like region. This analytic property shows that the soft mode of the QCD-CP is in the *space-like region*, and hence not conventional mesonic excitations in the time-like region.

Equation (3.34) is further expanded as

$$\Xi_S^{R\,-1}(\boldsymbol{k},\omega) \simeq\ a_S(T,\mu) + b_S|\boldsymbol{k}|^2 + c_S\frac{\omega}{|\boldsymbol{k}|}, \tag{3.36}$$

with $a_S(T,\mu) = G_S^{-1} + \lim_{|\boldsymbol{k}|\to 0} Q_S^R(\boldsymbol{k},0)$. We refer to Eq. (3.36) as the TDGL approximation for $\Xi_S^R(\boldsymbol{k},\omega)$ in analogy with Eq. (3.28). In contrast to the case for the 2SC-PT, Eqs. (3.34) or (3.36) is applicable only to the space-like region. When we use it, we thus assume $\Xi_S^R(\boldsymbol{k},\omega) = 0$ in the time-like region. The last term in Eq. (3.36) is finite in the space-like region.

The parameter $a_S(T,\mu)$ in Eq. (3.36) vanishes at the QCD-CP as in the case of 2SC-PT. Its behavior around there is, however, more intricate than the case of the 2SC-PT: When T and μ approach the QCD-CP linearly but with a different fixed ratio $T - T_{\rm CP} : \mu - \mu_{\rm CP}$ as [35], it varies differntly; for instance,

$$a_S \sim \begin{cases} \epsilon_{\rm CP} & \text{parallel to the first-order line,} \\ \epsilon_{\rm CP}^{2/3} & \text{otherwise,} \end{cases} \tag{3.37}$$

in the MFA with

$$\epsilon_{\rm CP} = \sqrt{\left(\frac{T - T_{\rm CP}}{T_{\rm CP}}\right)^2 + \left(\frac{\mu - \mu_{\rm CP}}{\mu_{\rm CP}}\right)^2}. \tag{3.38}$$

4. Emergence of pseudogap in quark excitation spectra

In the previous sections, we have seen that the fluctuations of Δ and M are enhanced near the 2SC-PT and QCD-CP, respectively, and well-developed collective modes, the soft modes, are formed, which become massless at the critical points of the second-order nature. The emergence of the soft modes can in turn naturally modify properties of various physical observables near the transition

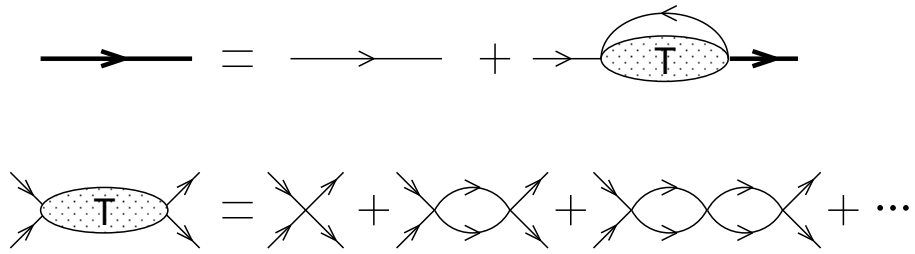

Figure 3. Feynman diagrams representing the quark Green function in the non-self-consistent T-matrix approximation. The thin lines represent the free propagator $\mathcal{G}_0$, while the bold ones represent the full propagator $\mathcal{G}$.

points. In this and the next sections, we investigate some such observables in the dense quark matter near the 2SC-PT and QCD-CP.

In this section, we focus on the modification of the excitation properties of quarks due to the soft modes. In the strongly correlated superconductors, such as the high-temperature superconductors and cold atoms near the unitarity limit, it is known that there appear unconventional properties in the fermionic excitations near the critical temperature T_c. They lead to the suppression of the density of states near the Fermi surface even above the critical temperature, which is called the pseudogap phenomenon. In this section, we explore the possibility of the appearance of the pseudogap in the quark spectral function near the 2SC-PT and QCD-CP.

The excitation properties of quarks are contained in the one-particle quark spectral function,

$$\mathcal{A}(\boldsymbol{k},\omega) = -\frac{1}{\pi}\cdot \mathrm{Im}G^R(\boldsymbol{k},\omega) = -\frac{1}{\pi}\frac{G^R(\boldsymbol{k},\omega)-\gamma^0 G^{R\dagger}(\boldsymbol{k},\omega)\gamma^0}{2i}, \tag{4.39}$$

with the retarded quark Green's function $G^R(\boldsymbol{k},\omega)$. From rotational and parity invariance, the Dirac indices of $\mathcal{A}(\boldsymbol{k},\omega)$ can be decomposed into

$$\mathcal{A}(\boldsymbol{k},\omega) = \rho_0(\boldsymbol{k},\omega)\gamma^0 - \rho_{\mathrm{v}}(\boldsymbol{k},\omega)\hat{\boldsymbol{k}}\cdot\boldsymbol{\gamma} + \rho_{\mathrm{s}}(\boldsymbol{k},\omega), \tag{4.40}$$

with $\hat{\boldsymbol{k}} = \boldsymbol{k}/|\boldsymbol{k}|$. Here, $\rho_0(\boldsymbol{k},\omega)$ represents the strength of the quark number, and the DOS of the quarks is defined through this channel as

$$N(\omega) = 4\int \frac{d^3\boldsymbol{k}}{(2\pi)^3}\mathrm{Tr}_{\mathrm{c,f}}[\rho_0(\boldsymbol{k},\omega)], \tag{4.41}$$

with $\mathrm{Tr}_{\mathrm{c,f}}$ denoting the trace over color and flavor indices.

To calculate the quark Green's function by incorporating the effects of the soft modes of the 2SC-PT, we employ the non-self-consistent T-matrix approximation [25,53], where the quark propagator is diagrammatically represented as in Fig. 3. The thin and bold lines in the figure represent the free and full propagators. In the Matsubara formalism, the quark self-energy in this approximation is given by

$$\tilde{\Sigma}(\boldsymbol{p},\omega_n) = -4\sum_{A=2,5,7}(\lambda_A)^2 T\sum_m \int \frac{d^3\boldsymbol{k}}{(2\pi)^3}\tilde{\Xi}_D(\boldsymbol{p}+\boldsymbol{k},\omega_n+\omega'_m)\mathcal{G}_0(\boldsymbol{k},\omega'_m), \tag{4.42}$$

where $\tilde{\Xi}_D(\boldsymbol{p},\nu_n)$ is the T-matrix in the imaginary-time formalism. In Eq. (4.42), effects of the diquark soft modes are contained in the propagation of quarks through the T-matrix.

In Fig. 4, we show the spectral function $\rho_0(\boldsymbol{k},\omega)$ obtained in this approximation near the 2SC-PT at $\mu = 400$MeV and $\varepsilon = 0.01$ (left) and 0.2 (right) with $\varepsilon = (T-T_{\mathrm{c}})/T_{\mathrm{c}}$. One sees clear peak structures around $\omega = \pm k - \mu$ in both figures, which correspond to the quasi-quark and anti-quark excitations, respectively. The quasi-quark peak has a clear depression around the Fermi energy $\omega = 0$, which means that the decay rate of quark excitations is enhanced there. The depression becomes more

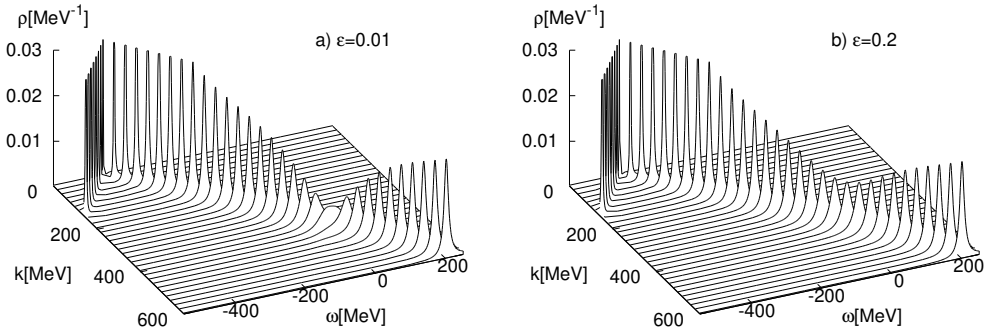

Figure 4. The spectral function ρ_0 at $\mu = 400$MeV and $\varepsilon = 0.01$ and 0.2. The upper figure is an enlargement of that near the Fermi surface [53]. The peaks at $\omega = k - \mu$ and $\omega = -k - \mu$ correspond to the quark and anti-quark quasiparticles, respectively. Notice that there is a depression around $\omega = 0$, which is responsible for the pseudogap formation.

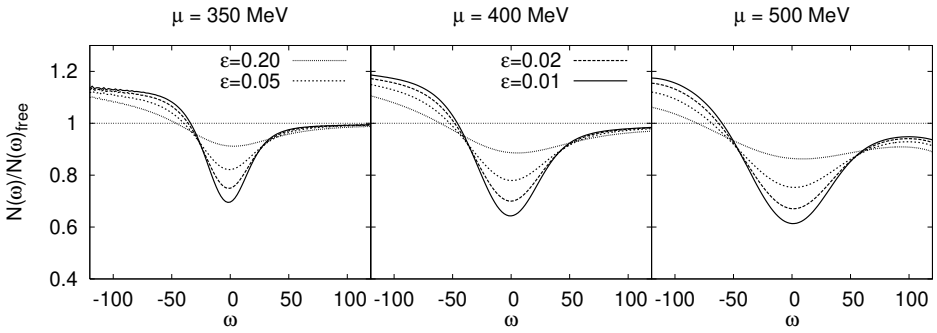

Figure 5. Density of state at $\mu = 400$MeV and various $\varepsilon \equiv (T - T_c)/T_c$ [53]. The Dotted line shows that of the free quarks. A clear pseudogap structure is seen, which survives up to $\varepsilon \approx 0.05$.

remarkable as ϵ decreases. This behavior is in contrast to that of the conventional Fermi liquid, in which the lifetime of the quasiparticles becomes longer as ω approaches the Fermi energy.

Substituting this spectral function into Eq. (4.41), one obtains the quark DOS $N(\omega)$. In Fig. 5, we show the DOS normalized by that of the free quarks, $N_{\rm free}(\omega) = 2N_{\rm f}N_{\rm c}(\omega - \mu)^2/\pi^2$, for $\mu = 350, 400, 500$ MeV and several values of ϵ [53]. There appears clear depression in the DOS around the Fermi energy for $\epsilon = 0.01$ for all μ, and the depression survives up to $\epsilon \approx 0.05$. This result shows the pseudogap phenomenon of the color superconductivity. The appearance of the pseudogap in the quark DOS is naturally understood through the non-Fermi liquid behaviors in $\rho_0(\boldsymbol{k}, \omega)$ and $\omega = \omega_-(\boldsymbol{k})$ shown for the first time in [25,53].

Similar pseudogap phenomena owing to the soft modes of the QCD-CP have been explored in Ref. [54]. In this case, however, it was found that the quark spectrum has an intricate rich structure. In a thermal relativistic system, it is known that a simple boson-exchange interaction leads to the mass gap in fermionic excitations, called the thermal mass. When the boson that couples to the fermions is massless, the fermionic excitation has two branches, one of which is called the plasmino. It is also known that the case where the boson mass is nonzero, the fermionic spectrum exhibits three-peak structure; in addition to the normal and plasmino modes, there emerges almost massless mode. In Ref. [55,56], the emergence of such a three-peak structure is confirmed near the chiral phase transition in the chiral limit. The analysis is then extended to the QCD-CP in Ref. [54]; see also [57,58] for the case of $\mu = 0$.

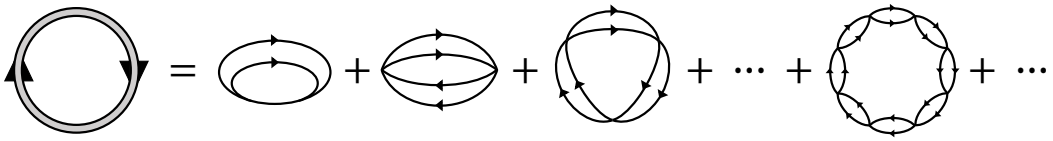

Figure 6. Contribution of the diquark soft mode to the thermodynamic potential.

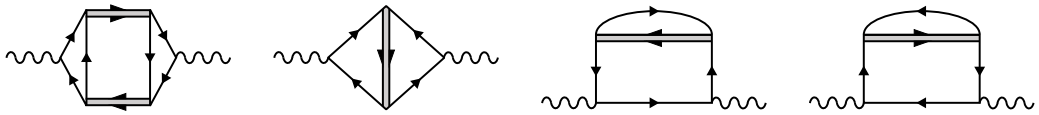

(a) (b) (c) (d)

Figure 7. Diagrammatic representations of the Aslamazov-Larkin (a), Maki-Thompson (b) and density of states (c, d) terms with the 2SC soft modes with the wavy lines being the photon ones.

5. Electric conductivity and dilepton production rates

In this section, we explore the effects of the soft modes on the electric conductivity and dilepton production rates (DPR) near the 2SC-PT and QCD-CP. These quantities are derived from the retarded photon self-energy

$$\Pi^{R\mu\nu}(\boldsymbol{k},\omega) = \int d^4x e^{i\omega t - i\boldsymbol{k}\cdot\boldsymbol{x}} \langle [j^\mu(\boldsymbol{x},t), j^\nu(\boldsymbol{0},0)] \rangle \theta(t), \tag{5.43}$$

with the electric current operator $j^\mu(\boldsymbol{x},t)$. The electric conductivity σ is given by the low-energy limit of Eq. (5.43) as

$$\sigma = -\frac{1}{3}\lim_{\omega\to 0}\frac{1}{\omega}\sum_{i=1}^{3}\mathrm{Im}\Pi^{Rii}(\boldsymbol{0},\omega), \tag{5.44}$$

and the DPR is related to $\Pi^{R\mu\nu}(\boldsymbol{k},\omega)$ as

$$\frac{d^4\Gamma}{d^4k} = -\frac{\alpha}{12\pi^4}\frac{1}{k^2}\frac{1}{e^{\omega/T}-1}g_{\mu\nu}\mathrm{Im}\Pi^{R\mu\nu}(k), \tag{5.45}$$

where α is the fine structure constant.

In this section, we first construct the photon self-energy $\Pi^{R\mu\nu}(\boldsymbol{k},\omega)$ by incorporating the soft modes so as to satisfy the *Ward-Takahashi (WT) identity*, and then derive the electric conductivity and DPR from it. Throughout this section, we assume that $\Pi^{R\mu\nu}(\boldsymbol{k},\omega)$ consists of three parts

$$\Pi^{R\mu\nu}(\boldsymbol{k},\omega) = \Pi^{R\mu\nu}_{\mathrm{free}}(\boldsymbol{k},\omega) + \Pi^{R\mu\nu}_{D}(\boldsymbol{k},\omega) + \Pi^{R\mu\nu}_{S}(\boldsymbol{k},\omega), \tag{5.46}$$

where $\Pi^{R\mu\nu}_{D}(\boldsymbol{k},\omega)$ and $\Pi^{R\mu\nu}_{S}(\boldsymbol{k},\omega)$ represent the contributions from the soft modes of the 2SC-PT and QCD-CP, respectively, that will be defined below and $\Pi^{R\mu\nu}_{D}(\boldsymbol{k},\omega)$ is the self-energy of the free-quark system. In the Matsubara formalism, it is given by

$$\tilde{\Pi}^{\mu\nu}_{\mathrm{free}}(k) = N_c C_{\mathrm{em}}\int_p \mathrm{Tr}_D[\gamma^\mu \mathcal{G}_0(p+k)\gamma^\nu \mathcal{G}_0(p)], \tag{5.47}$$

where $e_u = 2|e|/3$ ($e_d = -|e|/3$) is the electric charge of the up (down) quark with e being the electron charge and $C_{\mathrm{em}} \equiv e_u^2 + e_d^2$.

5.1. Photon self-energy

5.1.1. Contribution of the soft modes of 2SC-PT

Let us first investigate $\Pi_D^{R\mu\nu}(\boldsymbol{k},\omega)$, which represents the effects of the soft modes of the 2SC-PT. To construct it in a gauge-invariant manner, we start with the lowest contribution of the soft modes to the thermodynamic potential

$$\Omega_D = 3\int_p \ln[G_D\tilde{\Xi}_D^{-1}(p)], \tag{5.48}$$

which is the one-loop diagram of $\tilde{\Xi}_D(p)$. The graphical representation of Eq. (5.48) is given in Fig. 6, where $\tilde{\Xi}_D(p)$ is the imaginary-time T-matrix corresponding to Eq. (3.16) and the overall coefficient 3 comes from three anti-symmetric channels of the diquark modes.

The photon self-energy satisfying the WT identity is then constructed by attaching electromagnetic vertices at any two points on the quark lines in Ω_D. This procedure leads to the four types of diagrams shown in Fig. 7; they are called (a) Aslamazov-Larkin (AL) [36], (b) Maki-Thompson (MT) [37,38], and (c, d) density of states (DOS) terms, respectively, in the theory of metallic superconductivity [39]. In the Matsubara formalism we have

$$\tilde{\Pi}_D^{\mu\nu}(k) = \tilde{\Pi}_{\mathrm{AL},D}^{\mu\nu}(k) + \tilde{\Pi}_{\mathrm{MT},D}^{\mu\nu}(k) + \tilde{\Pi}_{\mathrm{DOS},D}^{\mu\nu}(k), \tag{5.49}$$

where

$$\tilde{\Pi}_{\mathrm{AL},D}^{\mu\nu}(k) = 3\int_q \tilde{\Gamma}_D^{\mu}(q,q+k)\tilde{\Xi}_D(q+k)\tilde{\Gamma}_D^{\nu}(q+k,q)\tilde{\Xi}_D(q), \tag{5.50}$$

$$\tilde{\Pi}_{\mathrm{MT\ (DOS)},D}^{\mu\nu}(k) = 3\int_q \tilde{\Xi}_D(q)\ \mathcal{R}_{\mathrm{MT\ (DOS)},D}^{\mu\nu}(q,k), \tag{5.51}$$

denote the contributions of the AL, MT, and DOS terms, respectively, with the vertex functions

$$\tilde{\Gamma}_D^{\mu}(q,q+k) = 4(N_c-1)e_\Delta\int_p \mathrm{Tr}_D[\mathcal{G}_0(p)\gamma^\mu\mathcal{G}_0(p+k)\mathcal{G}_0(q-p)], \tag{5.52}$$

$$\mathcal{R}_{\mathrm{MT},D}^{\mu\nu}(q,k) = 8(N_c-1)\ e_u e_d\int_p \mathrm{Tr}_D[\mathcal{G}_0(p)\gamma^\mu\mathcal{G}_0(p+k)\mathcal{G}_0(q-p-k)\gamma^\nu\mathcal{G}_0(q-p)], \tag{5.53}$$

$$\mathcal{R}_{\mathrm{DOS},D}^{\mu\nu}(q,k) = 4(N_c-1)(e_u^2+e_d^2)\sum_{s=\pm}\int_p \mathrm{Tr}_D[\mathcal{G}_0(p)\gamma^\mu\mathcal{G}_0(p+sk)\gamma^\nu\mathcal{G}_0(p)\mathcal{G}_0(q-p)], \tag{5.54}$$

and $q=(\boldsymbol{q},i\nu_n)$ representing the four-momentum of the soft mode. One can explicitly check that they satisfy the WT identities

$$k_\mu\tilde{\Gamma}_D^{\mu}(q,q+k) = (e_u+e_d)[\mathcal{Q}_D(q+k)-\mathcal{Q}_D(q)], \tag{5.55}$$

$$k_\mu\mathcal{R}_D^{\mu\nu}(q,k) = (e_u+e_d)[\tilde{\Gamma}_D^{\nu}(q-k,q)-\tilde{\Gamma}_D^{\nu}(q,q+k)], \tag{5.56}$$

with $\mathcal{R}_D^{\mu\nu}(q,k) = \mathcal{R}_{\mathrm{MT},D}^{\mu\nu}(q,k)+\mathcal{R}_{\mathrm{DOS},D}^{\mu\nu}(q,k)$. Using Eqs. (5.55) and (5.56), it is also verified that $\tilde{\Pi}^{\mu\nu}(k)$ satisfies the WT identity $k_\mu\tilde{\Pi}^{\mu\nu}(k)=0$.

In the following numerical analyses, we use the LE or TDGL approximation for $\tilde{\Xi}_D(q)$ in Eqs. (5.50) and (5.51). In this case, the vertices $\tilde{\Gamma}_D^{\mu}(q,q+k)$ and $\mathcal{R}_D^{\mu\nu}(q,k)$ are determined so as to satisfy Eqs. (5.55) and (5.56) with these approximated T-matrices. This procedure is most easily carried out with the low energy-momentum expansion of the vertices.

When the LE approximation is adopted, one can show that $\mathcal{R}_D^{\mu\nu}(q,k)$ is a real function of momentum only. Using this property, it is shown that

$$\mathrm{Im}\left[\Pi_{\mathrm{MT},D}^{Rij}(\boldsymbol{k},\omega)+\Pi_{\mathrm{DOS},D}^{Rij}(\boldsymbol{k},\omega)\right] = 0, \tag{5.57}$$

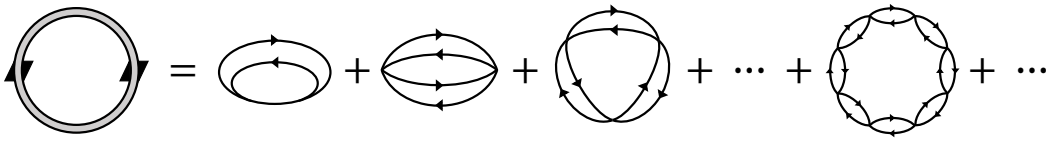

Figure 8. Contribution of the soft mode of the QCD-CP to the thermodynamic potential.

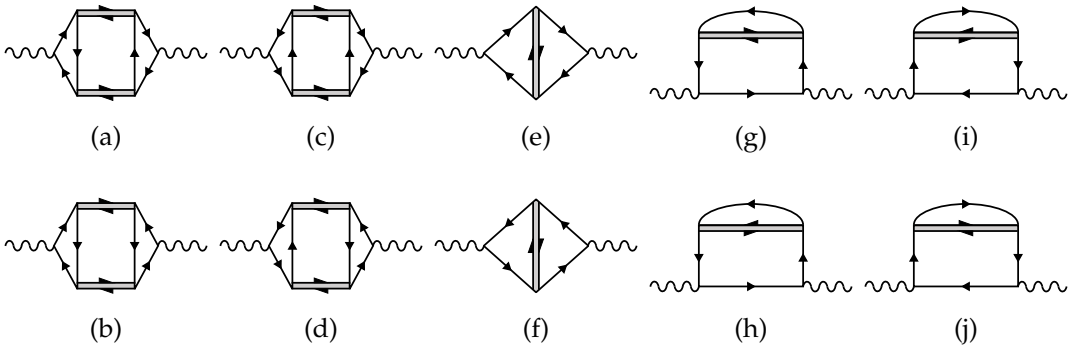

Figure 9. The diagrammatic representations of the Aslamazov-Larkin (a)–(d), Maki-Thompson (e, f) and density of states (g)–(j) terms with the soft modes of the QCD-CP. The single, double, and wavy lines are quarks, soft modes, and photon, respectively.

i.e., the MT and DOS terms cancel out exactly in $\mathrm{Im}\Pi^{Rij}(\boldsymbol{k},\omega)$ [59]. Since the electric conductivity and the DPR depend only on $\mathrm{Im}\Pi^{Rij}(\boldsymbol{k},\omega)$ as in Eqs. (5.44) and (5.45), Eq. (5.57) shows that only the AL term contribute to these quantities. The explicit form of $\mathrm{Im}\Pi^{Rij}_D(\boldsymbol{k},\omega)$ is obtained from Eq. (5.50) by taking the analytic continuation $i\nu_l \to \omega + i\eta$ as

$$\begin{aligned}\mathrm{Im}\Pi^{Rij}_D(\boldsymbol{k},\omega) &= \mathrm{Im}\Pi^{Rij}_{\mathrm{AL},D}(\boldsymbol{k},\omega)\\ &= 3\int\frac{d^3q}{(2\pi)^3}\Gamma^i_D(\boldsymbol{q},\boldsymbol{q}+\boldsymbol{k})\Gamma^j_D(\boldsymbol{q}+\boldsymbol{k},\boldsymbol{q})\int\frac{d\omega'}{2\pi}\coth\frac{\omega'}{2T}\\ &\quad \mathrm{Im}\Xi^R_D(\boldsymbol{q},\omega')\Big\{\mathrm{Im}\Xi^R_D(\boldsymbol{q}+\boldsymbol{k},\omega'+\omega)-\mathrm{Im}\Xi^R_D(\boldsymbol{q}-\boldsymbol{k},\omega'-\omega)\Big\}. \end{aligned} \tag{5.58}$$

5.1.2. Contribution of the soft modes of QCD-CP

Next, we calculate $\Pi^{R\mu\nu}_S(\boldsymbol{k},\omega)$, i.e., the modification of the photon self-energy from the soft modes of the QCD-CP [27]. As the calculational procedure goes in a similar way to Sec. 5.1.1, duplicated descriptions will be omitted in what follows.

Similarly to the previous analysis, we start from the one-loop diagram of the soft mode of the QCD-CP shown in Fig. 8, which is the lowest-order contribution to the thermodynamic potential $\Omega_S = \int_p \ln[G_S\tilde{\Xi}_S^{-1}(p)]$. Attaching electromagnetic vertices at any different two points of quark lines in Ω_S, we obtain ten types of diagrams shown in Fig. 9, where the number of diagrams is larger than that in Fig. 7 because the directions of quark lines in the vertices should be distinguished in this case. We refer to the diagrams (a)–(d) as the AL, (e), (f) as the MT, and (g)–(j) as the DOS terms, respectively. The respective contributions to the photon self-energy in the imaginary-time formalism are denoted by

$$\tilde{\Pi}^{\mu\nu}_{\mathrm{AL},S}(k) = \sum_{f=u,d}\int_q \tilde{\Gamma}^\mu_f(q,q+k)\tilde{\Xi}_S(q+k)\tilde{\Gamma}^\nu_f(q+k,q)\tilde{\Xi}_S(q), \tag{5.59}$$

$$\tilde{\Pi}^{\mu\nu}_{\mathrm{MT},S}(k) = \sum_{f=u,d}\int_q \tilde{\Xi}_S(q)\ \mathcal{R}^{\mu\nu}_{\mathrm{MT},f}(q,k), \tag{5.60}$$

$$\tilde{\Pi}^{\mu\nu}_{\mathrm{DOS},S}(k) = \sum_{f=u,d}\int_q \tilde{\Xi}_S(q)\ \mathcal{R}^{\mu\nu}_{\mathrm{DOS},f}(q,k), \tag{5.61}$$

which in total gives $\tilde{\Pi}_S^{\mu\nu}(k)$ as

$$\tilde{\Pi}_S^{\mu\nu}(k) = \tilde{\Pi}_{\mathrm{AL},S}^{\mu\nu}(k) + \tilde{\Pi}_{\mathrm{MT},S}^{\mu\nu}(k) + \tilde{\Pi}_{\mathrm{DOS},S}^{\mu\nu}(k). \tag{5.62}$$

As before, one can explicitly check that the vertex functions in these equations satisfy the WT identities

$$k_\mu \tilde{\Gamma}_f^\mu(q, q+k) = -e_f[\tilde{\Xi}_S^{-1}(q+k) - \tilde{\Xi}_S^{-1}(q)], \tag{5.63}$$

$$k_\mu \mathcal{R}_f^{\mu\nu}(q,k) = -e_f[\tilde{\Gamma}_f^\nu(q-k,q) - \tilde{\Gamma}_f^\nu(q,q+k)], \tag{5.64}$$

with $\mathcal{R}_f^{\mu\nu}(q,k) = \mathcal{R}_{\mathrm{MT},f}^{\mu\nu}(q,k) + \mathcal{R}_{\mathrm{DOS},f}^{\mu\nu}(q,k)$. The WT identity of Eq. (5.62), $k_\mu \tilde{\Pi}_S^{\mu\nu}(k) = 0$, is easily verified using Eqs. (5.63) and (5.64).

As in the previous subsection, we use the LE or TDGL approximation for $\tilde{\Xi}_S(q)$ and determine the vertex functions $\tilde{\Gamma}_f^\mu(q, q+k)$ and $\mathcal{R}_f^{\mu\nu}(q,k)$ so that they satisfy Eqs. (5.63) and (5.64). One can then show that $\mathcal{R}_f^{ij}(q,k)$ is a real function only of momenta $\boldsymbol{q}$ and $\boldsymbol{k}$. Using this property and the same procedure as we did in Eq. (5.57), it is shown that the MT and DOS terms cancel out in the spatial components of $\mathrm{Im}\Pi_S^{R\mu\nu}(\boldsymbol{k},\omega)$. Thus $\mathrm{Im}\Pi_S^{Rij}(\boldsymbol{k},\omega)$ is again given solely by the AL term. The final result is calculated to be

$$\begin{aligned}
\mathrm{Im}\Pi_S^{Rij}(\boldsymbol{k},\omega) &= \mathrm{Im}\Pi_{\mathrm{AL},S}^{Rij}(\boldsymbol{k},\omega) \\
&= \sum_f \int \frac{d^3q}{(2\pi)^3} \Gamma_f^i(\boldsymbol{q}, \boldsymbol{q}+\boldsymbol{k}) \Gamma_f^j(\boldsymbol{q}+\boldsymbol{k}, \boldsymbol{q}) \int \frac{d\omega'}{2\pi} \coth\frac{\omega'}{2T} \\
&\times \mathrm{Im}\Xi_S^R(\boldsymbol{q},\omega') \Big\{ \mathrm{Im}\Xi_S^R(\boldsymbol{q}+\boldsymbol{k}, \omega'+\omega) - \mathrm{Im}\Xi_S^R(\boldsymbol{q}-\boldsymbol{k}, \omega'-\omega) \Big\}.
\end{aligned} \tag{5.65}$$

5.2. Electric conductivity

Now, we apply the photon self-energy obtained above to the analysis of the electric conductivity σ. Since the photon self-energy consists of three contributions as given in Eq. (5.46), the spectral function at zero momentum $\rho(\omega) = -\sum_i \mathrm{Im}\Pi^{Rii}(\boldsymbol{0},\omega)$ is also decomposed as

$$\rho(\omega) = \rho_{\mathrm{free}}(\omega) + \rho_D(\omega) + \rho_S(\omega), \tag{5.66}$$

with $\rho_{\mathrm{free}}(\omega) = -\sum_i \mathrm{Im}\Pi_{\mathrm{free}}^{Rii}(\boldsymbol{0},\omega), \rho_D(\omega) = -\sum_i \mathrm{Im}\Pi_D^{Rii}(\boldsymbol{0},\omega), \rho_S(\omega) = -\sum_i \mathrm{Im}\Pi_S^{Rii}(\boldsymbol{0},\omega)$. Among them, $\rho_{\mathrm{free}}(\omega)$ does not contribute to σ since $\rho_{\mathrm{free}}(\omega) = 0$ for $|\omega| < 2M$. Near the 2SC-PT, $\rho_D(\omega)$ dominates over $\rho_S(\omega)$ and the behavior of σ is described solely by $\rho_D(\omega)$, and vice versa. In the following, therefore, we calculate the transport coefficients from $\rho_D(\omega)$ and $\rho_S(\omega)$ separately near the 2SC-PT and QCD-CP, respectively.

Before discussing the numerical results, it is instructive to explore the behaviors of σ near the 2SC-PT and QCD-CP analytically. From Eqs. (5.58) and (5.65), derivatives of $\rho_\gamma(\omega)$ ($\gamma = D, S$) at $\omega = 0$ are obtained as

$$\left.\frac{\partial^n \rho_\gamma(\omega)}{\partial^n \omega}\right|_{\omega=0} = 2\bar{N}_\gamma \int \frac{d^3q}{(2\pi)^3} |\boldsymbol{\Gamma}_\gamma(\boldsymbol{q},\boldsymbol{q})|^2 \int d\omega' \coth\frac{\omega'}{2T} \mathrm{Im}\Xi_\gamma^R(\boldsymbol{q},\omega') \frac{\partial^n}{\partial^n \omega'} \mathrm{Im}\Xi_\gamma^R(\boldsymbol{q},\omega'), \tag{5.67}$$

with $\bar{N}_D = 3e_\Delta^2$, $|\boldsymbol{\Gamma}_D(\boldsymbol{q},\boldsymbol{q})|^2 = \sum_i \Gamma_D^i(\boldsymbol{q},\boldsymbol{q})^2$, $\bar{N}_S = e_u^2 + e_d^2$, and $|\boldsymbol{\Gamma}_D(\boldsymbol{q},\boldsymbol{q})|^2 = \sum_{i,f} \Gamma_f^i(\boldsymbol{q},\boldsymbol{q})^2$.

In the case of the 2SC-PT, as T approaches T_c the integrand in Eq. (5.67) diverges at $(|\boldsymbol{q}|,\omega') = (0,0)$ owing to $a_D \to 0$ in this limit. Hence, the dominant contribution to Eq. (5.67) comes from the origin. This justifies the use of the TDGL approximations (3.28) and one obtains

$$\sigma = -\frac{3e_\Delta^2 T}{16\pi} \frac{1}{a_D^{1/2} b_D^{1/2}} \frac{|c_D|^2}{\mathrm{Im}c_D} \sim T\epsilon^{-1/2}. \tag{5.68}$$

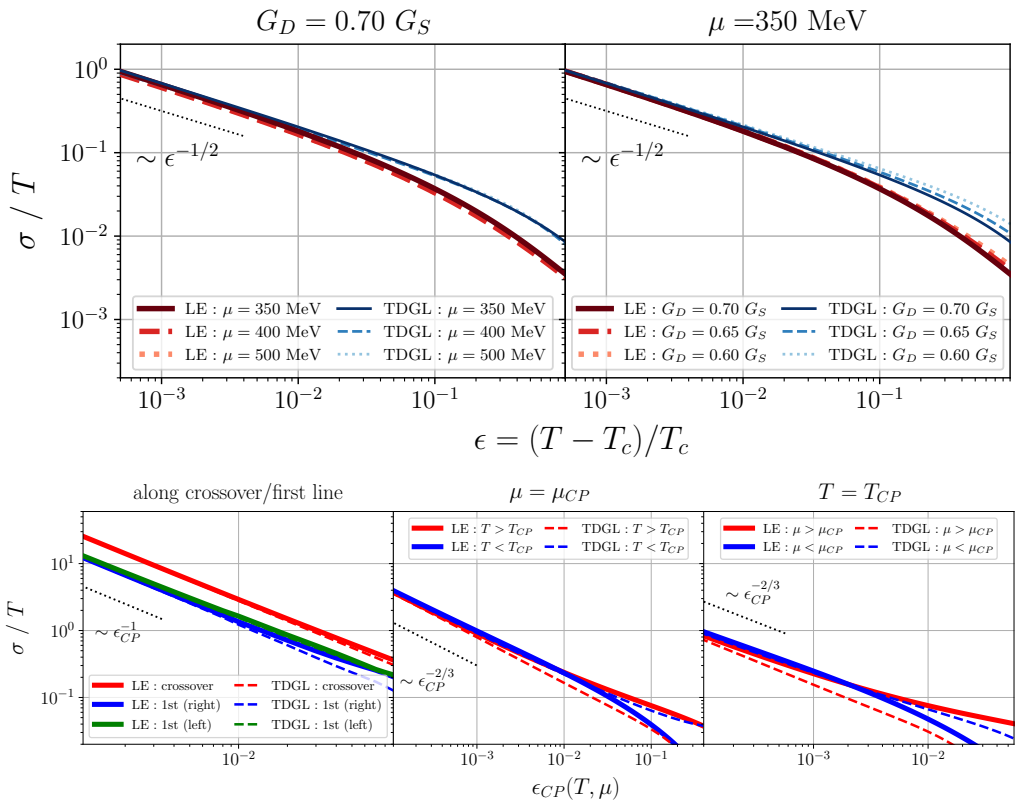

Figure 10. The upper panels: Electric conductivity σ near the 2SC-PT for several values of μ and G_D. The thick-red and thin-blue lines are the results of the LE and TDGL approximations, respectively. In the left panels, the lines are plotted at $\mu = 350$, 400, and 500 MeV with fixed $G_D/G_S = 0.7$, while the right panels show the results at $G_D/G_S = 0.70$, 0.65, and 0.60 for $\mu = 350$ MeV. The dotted lines indicate the critical exponents $\epsilon^{-1/2}$.
The lower panels: Electric conductivity σ near the QCD-CP. In the left panels, T and μ are varied along the transition line. The middle and right panels show the results with fixed $\mu = \mu_{\rm CP}$ and $T = T_{\rm CP}$, respectively. The dotted line in each panel represents the critical exponents in Eqs. (5.70).

This result shows that σ diverges at $T = T_{\rm c}$ with the critical exponent $-1/2$, which corresponds to the mean-field value. Equation (5.68) also tells us that the magnitude of σ does not have any explicit dependence on μ nor G_D, implying that σ is insensitive to μ around the 2SC-PT.

Next, we consider the case of the QCD-CP. In this case, the use of the TDGL approximation (3.36) leads to

$$\left.\frac{\partial \rho_S(\omega)}{\partial \omega}\right|_{\omega=0} = \frac{(e_u^2 + e_d^2)T}{2\pi^3}\frac{{\rm Im}c_S}{a_S}\tan^{-1}\frac{{\rm Im}c_S}{a_S}. \tag{5.69}$$

Using Eq. (3.37), we then obtain asymptotic behaviors

$$\sigma \sim \frac{1}{a_S} \sim \begin{cases} \epsilon_{\rm CP}^{-1} & \text{along the first-order PT or crossover transition lines,} \\ \epsilon_{\rm CP}^{-2/3} & \text{otherwise.} \end{cases} \tag{5.70}$$

Next, let us examine the numerical behavior of σ near the 2SC-PT and QCD-CP. The top panel of Fig. 10 shows σ/T as a function of $\epsilon = (T - T_{\rm c})/T_{\rm c}$. The left panels show the results for $\mu = 350, 400, 500$ MeV with fixed $G_D/G_S = 0.7$, while the value of G_D is varied at $\mu = 350$ MeV in the right panels. The thick-red (thin-blue) lines show the results in the LE (TDGL) approximation: One can see that σ/T grows as T approaches $T_{\rm c}$ with the exponents in Eq. (5.68) indicated by the dotted lines in the figure. One also sees that the LE and TDGL results tend to approach each other in this limit, while

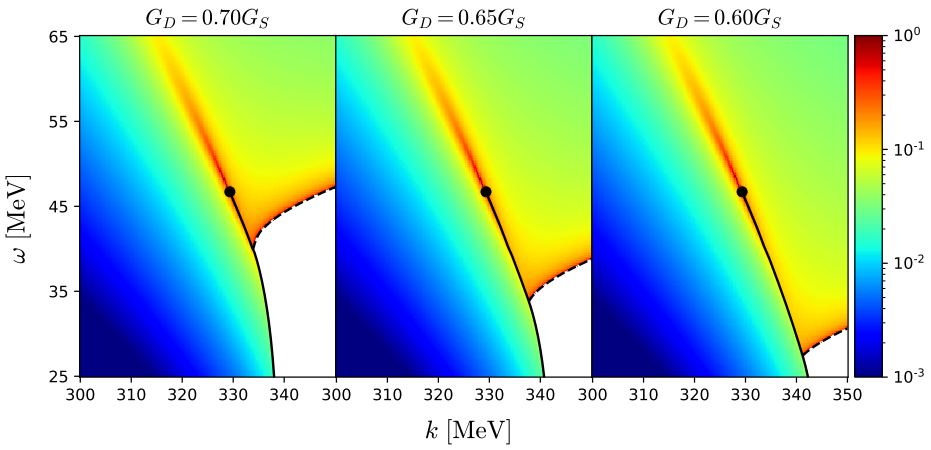

Figure 11. Contour maps of σ/T on the T–μ plane around the CP with $G_D/G_S = 0.70$, 0.65 and 0.60. The solid and dashed lines are the first-order and second-order phase transitions, respectively.

their difference grows as ϵ becomes larger. The figure confirms that σ/T is insensitive to μ and G_D, in accordance with the analytical results in Eq. (5.68).

In the lower panel of Fig. 10, we show the numerical results for the QCD-CP as functions of $\epsilon_{\rm CP}$ [35]. In the left panels, T and μ are varied along the phase transition line. For the first-order transition side, the results on the transition line are shown for the two coexisting states. For the crossover side with $T > T_{\rm CP}$, the transition line is defined by the point at which the chiral susceptibility, $\chi_M = \partial^2\Omega/\partial M^2$, takes the maximum for a given temperature T. In the middle panels, we set $\mu = \mu_{\rm CP}$ and vary T, while in the right panels μ is varied with fixed $T = T_{\rm CP}$. The thick and thin lines are the results in the LE and TDGL approximations, respectively. The thin-dotted lines indicate the critical exponents in Eqs. (5.70). We see that the numerical results are in good agreement with the analytical results near the QCD-CP.

Figure 11 shows a summarizing global behavior of σ/T as a function of T and μ when the effects of the QCD-CP and 2SC-PT are included, simultaneously; the color maps show the results for three values of the diquark couplings $G_D/G_S = 0.70$, 0.65 and 0.60, respectively, in the LE approximation [35]. The solid and dashed lines denote the first-order transition and the second-order 2SC-PT, respectively. Since our formalism is not applicable to the 2SC phase with $\Delta \neq 0$, this phase is left blank in the figure. One finds that σ/T is enhanced around the QCD-CP and 2SC-PT. A significant enhancement due to the presence of the QCD-CP occurs along the critical line parallel to the first-order transition line. The existence of two isolated regions of the enhancement of σ is interesting in light of the beam-energy scan in the HIC, as it would result in two non-monotonic behaviors of an experimental observable as a function of the collision energy. We will come back to this point in the next subsection.

5.3. Dilepton production rates

Finally, we focus on the DPR, which is an experimental observable in the HIC. As the DPR is extracted from the photon self-energy as in Eq. (5.45), we calculate it using $\Pi^{{\rm R}ij}(\boldsymbol{k}, \omega)$ obtained in Sec. 5.1.

The left panel of Fig. 12 shows the DPR per unit energy ω and momentum $\boldsymbol{k}$ near the 2SC-PT for $T/T_c = 1.01$, 1.1 and 1.5 at $\mu = 350$ MeV and $G_D = 0.7G_S$ with the critical temperature $T_c = 42.94$ MeV [26]. The thick lines are the contributions from the soft modes, while the thin lines are the ones of the free quark gas. One sees that the DPR from the soft modes is anomalously enhanced at small ω and $\boldsymbol{k}$ region in comparison with the free quark gas for $T \lesssim 1.5T_c$, and this enhancement is more pronounced as T approaches T_c. This result is expected from the properties of the soft modes.

In HIC, the DPR is observed as a function of the invariant mass $M = \sqrt{\omega^2 - \boldsymbol{k}^2}$ to remove the effects of the motion of the medium. Shown in Fig. 13 is the invariant-mass spectra of DPR near the

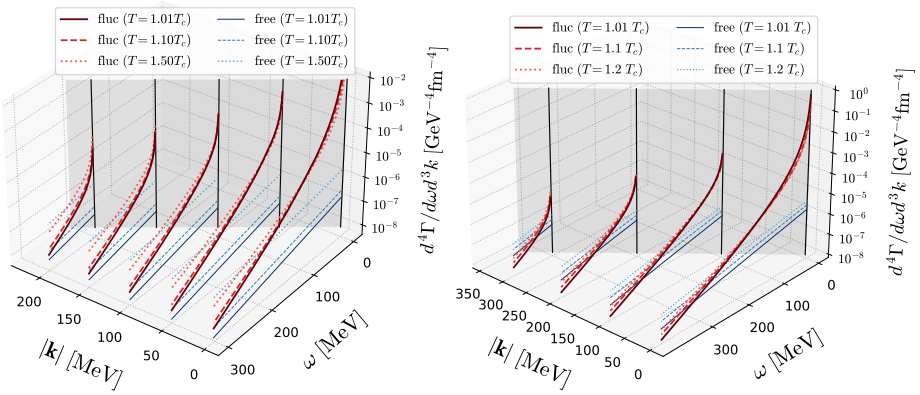

Figure 12. Dilepton production rates per unit energy ω and momentum $\boldsymbol{k}$ above T_c of the 2SC at $\mu = 350$ MeV (left) [26] and of the QCD-CP at $\mu = \mu_{\rm CP}$ (right) [27] with $G_D = 0.7G_S$. The thick (thin) lines are the contribution of the soft modes (the massless free quark gases).

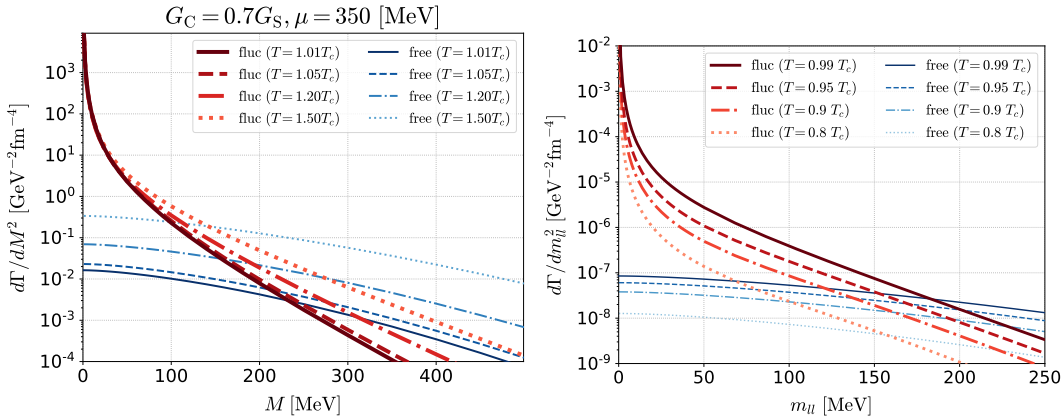

Figure 13. Dilepton production rates per unit energy ω and momentum $\boldsymbol{k}$ above T_c of the 2SC at $\mu = 350$ MeV (left) [26] and of the QCD-CP at $\mu = \mu_{\rm CP}$ (right) [27] with $G_D = 0.7G_S$. The thick (thin) lines are the contribution of the soft modes (the massless free quark gases).

2SC-PT (left) and QCD-CP (right) [27]. One finds that the anomalous enhancement of the DPR is observed at the low-mass region $M \lesssim 200$ MeV.

The low-energy-momentum limit of the DPR is related to the electric conductivity as is verified in Eqs. (5.44) and (5.45). Therefore, the dilepton production in the HIC is enhanced when the medium created by the collisions passes through the red color region in the figure [26,27]. The existence of the two hot spots, corresponding to the 2SC-CP and QCD-CP, in Fig. 11 may suggest that the beam-energy scan can measure distinct peaks of the DPR [59].

6. Brief summary and concluding remark

In this article, we have made a unified account of the soft modes of QCD-CP and 2SC-CP and their relevance to HIC, based on the 2-flavor Nambu-Jona-Lasinio (NJL) model. We started by discussing not only static but also dynamical fluctuations of physical quantities coupled to the order parameters of both the second-order phase transitions in the normal phase in a comprehensive way, and then showed the very existence of the soft modes for both the transitions within the mean-field level calculations. Then it was demonstrated that the soft modes affect various observables and cause interesting phenomena. Firstly, it was shown that the diquark soft mode of the 2SC give rise to a 'pseudogap' in the quark density of states around the Fermi surface in the normal phase just above the critical temperature of the 2SC. Although the appearance of the pseudogap is of great interest in relation to the similar phenomena seen in condensed matter physics, it is left as a future problem to identify good observables to confirm it experimentally. As experimentally feasible observables, we took up the electromagnetic observables, such as electric conductivity and the dilepton production rate in heavy-ion collisions, and showed that these quantities are largely affected by the soft modes so that they both get to increase in a divergent way when the system approaches the respective critical temperature from the normal phase. For that, we have extended the ideas that are successful for account for the 'para-conductivity' in the normal phase of metal superconductivity. In passing, we remark that the soft modes also cause an interesting anomalous behavior of the relaxation times [35].

Author Contributions:

Both authors contributed equally to shaping the project and research plan. M. K made the major contribution to the actual computations and made the Figures, and wrote the first draft of the main text except for Abstract, Introduction, and the last section, which were written by T.K. The authors equally contributed to finalizing the whole text of the paper.

Acknowledgments:

This work was partially supported in part by JSPS KAKENHI (No. 24K07049).

Conflicts of Interest:

The authors declare no conflicts of interest.

ma, K.; Hatsuda, T. The phase diagram of dense QCD. *Rept. Prog. Phys.* **2011**, *74*, 014001, [arXiv:hep-ph/1005.4814]. https:
g/10.1088/0034-4885/74/1/014001.
M.G.; Schmitt, A.; Rajagopal, K.; Schäfer, T. Color superconductivity in dense quark matter. *Rev. Mod. Phys.* **2008**, *80*, 1455–1515,
ep-ph/0709.4635]. https://doi.org/10.1103/RevModPhys.80.1455.
a, M.; Yazaki, K. Chiral Restoration at Finite Density and Temperature. *Nucl. Phys. A* **1989**, *504*, 668–684. https://doi.org/10.1016/03
(89)90002-X.
i, A.; Casalbuoni, R.; De Curtis, S.; Gatto, R.; Pettini, G. Chiral Symmetry Breaking in QCD at Finite Temperature and Density. *Phys.*
989, *231*, 463–470. https://doi.org/10.1016/0370-2693(89)90695-3.
a, M.; Koide, T.; Kunihiro, T.; Nemoto, Y. Chiral and color superconducting phase transitions with vector interaction in a simple
Prog. Theor. Phys. **2002**, *108*, 929–951, [hep-ph/0207255]. [Erratum: Prog.Theor.Phys. 110, 185–186 (2003)], https://doi.org/10.1143/
929.

o, T. Quark number susceptibility and fluctuations in the vector channel at high temperatures. *Phys. Lett. B* **1991**, *271*, 395–402. doi.org/10.1016/0370-2693(91)90107-2.
Hatsuda, T.; Miake, Y. *Quark-gluon plasma: From big bang to little bang*; Vol. 23, 2005.
k, T. Future facilities for high μ_B physics. *Nucl. Phys. A* **2019**, *982*, 163–169. https://doi.org/10.1016/j.nuclphysa.2018.11.025.
A.; Esumi, S.; Koch, V.; Liao, J.; Stephanov, M.; Xu, N. Mapping the Phases of Quantum Chromodynamics with Beam Energy Scan. *pt.* **2020**, *853*, 1–87, [arXiv:nucl-th/1906.00936]. https://doi.org/10.1016/j.physrep.2020.01.005.
h, M.; et al. Cumulants and correlation functions of net-proton, proton, and antiproton multiplicity distributions in Au+Au s at energies available at the BNL Relativistic Heavy Ion Collider. *Phys. Rev. C* **2021**, *104*, 024902, [arXiv:nucl-ex/2101.12413]. doi.org/10.1103/PhysRevC.104.024902.
ov, M.A.; Rajagopal, K.; Shuryak, E.V. Signatures of the tricritical point in QCD. *Phys. Rev. Lett.* **1998**, *81*, 4816–4819, [hep-ph/9806219]. doi.org/10.1103/PhysRevLett.81.4816.
, J.D. A Theory of highly condensed matter. *Annals Phys.* **1974**, *83*, 491–529. https://doi.org/10.1016/0003-4916(74)90208-5.
T. Fermi Liquid Properties of Nuclear Matter in a Relativistic Mean - Field Theory. *Nucl. Phys. A* **1981**, *370*, 365–388. https: g/10.1016/0375-9474(81)90103-2.
a, M.; Kitazawa, M. Fluctuations of conserved charges in relativistic heavy ion collisions: An introduction. *Prog. Part. Nucl. Phys.* 299–342, [arXiv:nucl-th/1512.05038]. https://doi.org/10.1016/j.ppnp.2016.04.002.
M.; et al. Dynamics of critical fluctuations: Theory – phenomenology – heavy-ion collisions. *Nucl. Phys. A* **2020**, *1003*, 122016, ucl-th/2001.08831]. https://doi.org/10.1016/j.nuclphysa.2020.122016.
Scalar density fluctuation at critical end point in NJL model. *Phys. Rev. D* **2003**, *67*, 094018, [hep-ph/0302167]. https://doi.org/10.1 sRevD.67.094018.
; Ohtani, M. Sigma and hydrodynamic modes along the critical line. *Phys. Rev. D* **2004**, *70*, 014016, [hep-ph/0402263]. https: g/10.1103/PhysRevD.70.014016.
T.; Kunihiro, T.; Morita, K. Functional renormalization group analysis of the soft mode at the QCD critical point. *PTEP* **2016**, 3D01, [arXiv:hep-ph/1603.02147]. https://doi.org/10.1093/ptep/ptw062.
T.; Kunihiro, T.; Morita, K. Tachyonic instability of the scalar mode prior to the QCD critical point based on the functional lization-group method in the two-flavor case. *Phys. Rev. D* **2017**, *96*, 074028, [arXiv:hep-ph/1707.05520]. https://doi.org/10.1103/ D.96.074028.
a, T.; Iida, K.; Hatsuda, T.; Baym, G. Thermal fluctuations of gauge fields and first order phase transitions in color superconductivity. *v. D* **2004**, *69*, 074012, [hep-ph/0312042]. https://doi.org/10.1103/PhysRevD.69.074012.
is, I.; Hou, D.f.; Ren, H.c.; Rischke, D.H. Gauge field fluctuations and first-order phase transition in color superconductivity. *Phys.* **2004**, *93*, 232301, [hep-ph/0406031]. https://doi.org/10.1103/PhysRevLett.93.232301.
a, J.L.; Ren, H.c.; Giannakis, I.; Hou, D.; Rischke, D.H. Absence of the London limit for the first-order phase transition to a color nductor. *Phys. Rev. D* **2006**, *73*, 094009, [hep-ph/0602218]. https://doi.org/10.1103/PhysRevD.73.094009.
.; Yamamoto, N. Functional renormalization group approach to color superconducting phase transition. *JHEP* **2019**, *12*, 069, ep-ph/1908.03535]. https://doi.org/10.1007/JHEP12(2019)069.
a, M.; Koide, T.; Kunihiro, T.; Nemoto, Y. Precursor of color superconductivity in hot quark matter. *Phys. Rev. D* **2002**, *65*, 091504, /0111022]. https://doi.org/10.1103/PhysRevD.65.091504.
a, M.; Koide, T.; Kunihiro, T.; Nemoto, Y. Pre-critical phenomena of two-flavor color superconductivity in heated quark matter: -pair fluctuations and non-Fermi liquid behavior. *Prog. Theor. Phys.* **2005**, *114*, 117–155, [hep-ph/0502035]. https://doi.org/10.1143/ 117.
ura, T.; Kitazawa, M.; Kunihiro, T. Anomalous enhancement of dilepton production as a precursor of color superconductivity. *PTEP* 22, 093D02, [arXiv:hep-ph/2201.01963]. https://doi.org/10.1093/ptep/ptac100.
ura, T.; Kitazawa, M.; Kunihiro, T. Enhancement of dilepton production rate and electric conductivity around the QCD critical point. **23**, *2023*, 053D01, [arXiv:hep-ph/2302.03191]. https://doi.org/10.1093/ptep/ptad051.
Y.; Jona-Lasinio, G. Dynamical Model of Elementary Particles Based on an Analogy with Superconductivity. 1. *Phys. Rev.* **1961**, -358. https://doi.org/10.1103/PhysRev.122.345.
Y.; Jona-Lasinio, G. Dynamical model of elementary particles based on an analogy with superconductivity. II. *Phys. Rev.* **1961**, -254. https://doi.org/10.1103/PhysRev.124.246.
; Weise, W. The Nambu and Jona Lasinio model: Its implications for hadrons and nuclei. *Prog. Part. Nucl. Phys.* **1991**, *27*, 195–272. doi.org/10.1016/0146-6410(91)90005-9.
ky, S.P. The Nambu-Jona-Lasinio model of quantum chromodynamics. *Rev. Mod. Phys.* **1992**, *64*, 649–708. https://doi.org/10.1103/ lPhys.64.649.
a, T.; Kunihiro, T. QCD phenomenology based on a chiral effective Lagrangian. *Phys. Rept.* **1994**, *247*, 221–367, [hep-ph/9401310]. doi.org/10.1016/0370-1573(94)90022-1.

.; Reinhardt, H.; Volkov, M.K. Effective hadron theory of QCD. *Prog. Part. Nucl. Phys.* **1994**, *33*, 1–120. https://doi.org/10.1016/0146)90043-4.
M. NJL model analysis of quark matter at large density. *Phys. Rept.* **2005**, *407*, 205–376, [hep-ph/0402234]. https://doi.org/10.1016/j.2004.11.004.
ura, T.; Kitazawa, M.; Kunihiro, T. Electromagnetic response of dense quark matter around color-superconducting phase transition D critical point. *Annals Phys.* **2024**, *469*, 169768, [arXiv:hep-ph/2405.09240]. https://doi.org/10.1016/j.aop.2024.169768.
zov, L.; Larkin, A. Soviet Solid State 10, 875 (1968). *Phys. Lett. A* **1968**, *26*, 238.
. Critical fluctuation of the order parameter in a superconductor. I. *Progress of Theoretical Physics* **1968**, *40*, 193–200.
on, R.S. Microwave, flux flow, and fluctuation resistance of dirty type-II superconductors. *Physical Review B* **1970**, *1*, 327.
A.; Varlamov, A. *Fluctuation phenomena in superconductors*; Springer, 2008; pp. 369–458.
n, M. *Introduction to superconductivity*; Courier Corporation, 2004.
P.B.; Moore, G.D.; Yaffe, L.G. Transport coefficients in high temperature gauge theories. 1. Leading log results. *JHEP* **2000**, *11*, 001, /0010177]. https://doi.org/10.1088/1126-6708/2000/11/001.
P.B.; Moore, G.D.; Yaffe, L.G. Transport coefficients in high temperature gauge theories. 2. Beyond leading log. *JHEP* **2003**, *05*, 051, /0302165]. https://doi.org/10.1088/1126-6708/2003/05/051.
D. Finite temperature spectral densities of momentum and R-charge correlators in N=4 Yang Mills theory. *Phys. Rev. D* **2006**, 25, [hep-ph/0602044]. https://doi.org/10.1103/PhysRevD.74.045025.
, W.; Linnyk, O.; Steinert, T.; Ozvenchuk, V. Electrical Conductivity of Hot QCD Matter. *Phys. Rev. Lett.* **2013**, *110*, 182301, ep-ph/1302.0906]. https://doi.org/10.1103/PhysRevLett.110.182301.
.; Bouras, I.; Greiner, C.; Xu, Z. Electric conductivity of the quark-gluon plasma investigated using a perturbative QCD based parton *Phys. Rev. D* **2014**, *90*, 094014, [arXiv:nucl-th/1408.7049]. https://doi.org/10.1103/PhysRevD.90.094014.
G.; Nikolaev, A. Electrical conductivity of the quark-gluon plasma: perspective from lattice QCD. *Eur. Phys. J. A* **2021**, *57*, 118, ep-lat/2008.12326]. https://doi.org/10.1140/epja/s10050-021-00436-5.
rek, O.; Shu, H.T. Spectral and Transport Properties from Lattice QCD. *Lect. Notes Phys.* **2022**, *999*, 307–345, [arXiv:hep-lat/2206.14676]. doi.org/10.1007/978-3-030-95491-8_8.
Y.; Hongo, M.; Hirano, T. Estimation of electric conductivity of the quark gluon plasma via asymmetric heavy-ion collisions. *Phys.* **014**, *90*, 021903, [arXiv:nucl-th/1211.1114]. https://doi.org/10.1103/PhysRevC.90.021903.
ura, K.; Miyoshi, T.; Nonaka, C.; Takahashi, H.R. Relativistic resistive magneto-hydrodynamics code for high-energy heavy-ion s. *Eur. Phys. J. C* **2023**, *83*, 229, [arXiv:nucl-th/2211.02310]. https://doi.org/10.1140/epjc/s10052-023-11343-y.
M.; Rezzolla, L.; Elfner, H.; Inghirami, G.; Rischke, D.H. BHAC-QGP: three-dimensional MHD simulations of relativistic heavy-ion s, II. Application to Au-Au collisions **2024**. [arXiv:hep-ph/2403.08669].
.L.; Walecka, J.D. *Quantum theory of many-particle systems*; Courier Corporation, 2012.
s, D.J. Perturbation theory in statistical mechanics and the theory of superconductivity. *Annals of Physics* **1960**, *10*, 553–588.
a, M.; Koide, T.; Kunihiro, T.; Nemoto, Y. Pseudogap of color superconductivity in heated quark matter. *Phys. Rev. D* **2004**, *70*, 056003, /0309026]. https://doi.org/10.1103/PhysRevD.70.056003.
a, M.; Kunihiro, T.; Nemoto, Y. Emergence of soft quark excitations by the coupling with a soft mode of the QCD critical point. *Phys.* **014**, *90*, 116008, [arXiv:hep-ph/1409.3733]. https://doi.org/10.1103/PhysRevD.90.116008.
a, M.; Kunihiro, T.; Mitsutani, K.; Nemoto, Y. Spectral properties of massless and massive quarks coupled with massive boson at finite ture. *Phys. Rev. D* **2008**, *77*, 045034, [arXiv:hep-ph/0710.5809]. https://doi.org/10.1103/PhysRevD.77.045034.
a, M.; Kunihiro, T.; Nemoto, Y. Novel Collective Excitations and Quasi-particle Picture of Quarks Coupled with a Massive Boson at mperature. *Prog. Theor. Phys.* **2007**, *117*, 103–138, [hep-ph/0609164]. https://doi.org/10.1143/PTP.117.103.
a, M.; Kunihiro, T.; Nemoto, Y. Quark spectrum above but near critical temperature of chiral transition. *Phys. Lett. B* **2006**, *633*, 269–274, /0510167]. https://doi.org/10.1016/j.physletb.2005.11.076.
a, M.; Kunihiro, T.; Nemoto, Y. Possible generation of anomalously soft quark excitations at nonzero temperature: Nonhyperbolic on of the parapion and van Hove singularity. *Phys. Rev. D* **2014**, *89*, 056002, [arXiv:hep-ph/1312.3022]. https://doi.org/10.1103/vD.89.056002.
ura, T.; Nara, Y.; Steinheimer, J. Enhanced Dilepton production near the color superconducting phase and the QCD critical point **2023**. ep-ph/2311.14135].